

Bacteria Inspired Multi-Flagella Propelled Soft Robot at Low Reynolds Number

Sangmin Lim,^{*} Achyuta Yadunandan,[†] and M. Khalid Jawed[‡]

Abstract

The locomotion and mechanical efficiency of micro organisms, specifically micro-swimmers, have drawn interest in the fields of biology and fluid dynamics. A challenge in designing flagellated micro- and macro-scale robots is the geometrically nonlinear deformation of slender structures (e.g. rod-like flagella) ensuing from the interplay of elasticity and hydrodynamics. Certain types of bacteria such as *Escherichia coli* propel themselves by rotating multiple filamentary structures in low Reynolds flow. This multi-flagellated propulsive mechanism is qualitatively different from the single-flagellated mechanism exhibited by some other types of bacteria such as *Vibrio cholerae*. The differences include the flagella forming a bundle to increase directional stability for cell motility, offering redundancy for a cell to move, and offering the ability of flagella to be the delivery material itself. Above all, multi-flagellated biological system can inspire novel soft robots for application in drug transportation and delivery within the human body. We present a macroscopic soft robotic hardware platform and a computational framework for a physically plausible simulation model of the multi-flagellated robot. The fluid-structure interaction simulation couples the Discrete Elastic Rods algorithm with the method of Regularized Stokeslet Segments. Contact between two flagella is handled by a penalty-based method due to Spillmann and Teschner. We present comparison between our experimental and simulation results and verify that the simulation tool can capture the essential physics of this problem. The stability and efficiency of a multi-flagellated robot are compared with the single-flagellated counterpart.

Keywords: Discrete Elastic Rod, Soft Robotics, Bacteria-inspired Robot

1. Introduction

Locomotion of micro-swimmers has drawn significant attention in biology and fluid dynamics since the 1950s.^{1–6} A seminal paper by Purcell in 1977 introduced the counter intuitive behavior of cell locomotion in low Reynolds flow where viscosity dominates over inertial effects.⁵ In this regime, the so called scallop theorem elaborates reciprocal motions do not provide propulsive force. In order to overcome this constraint, several micro-swimmers in nature use elastic corkscrew like structures, or flagella, to propel themselves forward. It was also found that monotrichous bacteria, or single flagellated bacteria, such as *Vibrio cholerae* exploit buckling instability in the flagel-

lum to make directional change in their motion.⁷ Consequently, numerous biological findings,^{2,8–13} mechanical experiments,^{14,15} hydrodynamic theories for low Reynolds flow,^{1,3,5,16,17} and medical microbots^{18–21} explored and exploited such a mechanism.

Multi-flagellated locomotion displays fundamentally different mechanism from monotrichous locomotion. There are two modes for the former type of locomotion: “run” and “tumble”.^{2,9,10} For example, *Escherichia coli*, flagella are formed as left-handed helices.²² Run is a period of near straight line motion that is caused by bundling of flagella. As multiple flagella turn in the same direction (counter clock wise (CCW) for *E. coli*),

^{*}Department of Mechanical and Aerospace Engineering, University of California, Los Angeles, California, USA.

[†]Department of Electrical and Computer Engineering, University of California, Los Angeles, California, USA.

[‡]Department of Mechanical and Aerospace Engineering, University of California, Los Angeles, California, USA.

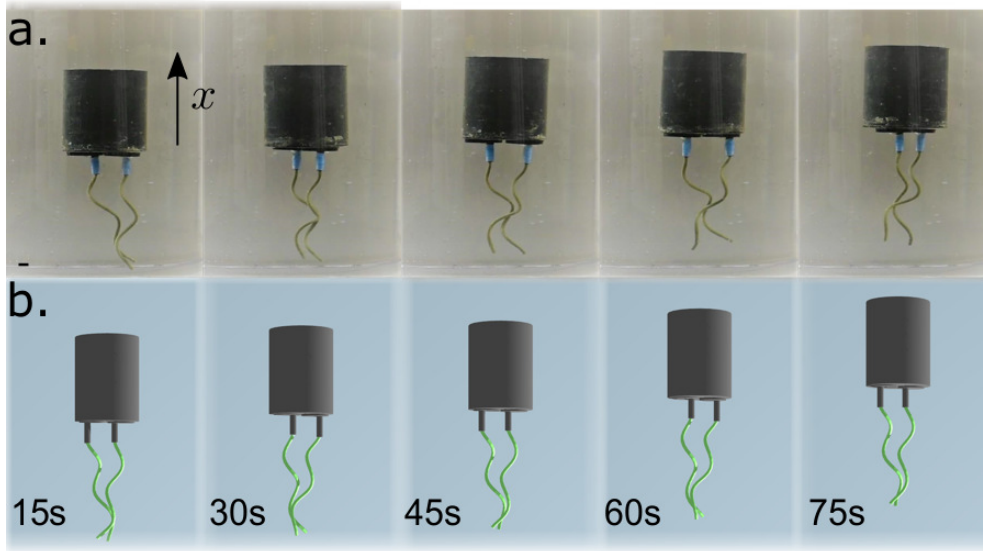


Figure 1. Snapshots (at 15 second increments) from (a) experiments and (b) simulations of a flagellated robot with a motor frequency of 60 rpm. The two flagella are made of elastomeric (Vinyl Polysiloxane) rods. The normalized pitch to helix radius ratio ($\bar{\lambda}$) is 9. Arrow representing global x-axis is noted. Scale bar : 1 cm. See Table 1 for the physical parameters.

they form a single or multiple bundles of helical shape. On the other hand, tumble is a period of random directional change which is caused by change in rotational direction of flagella i.e. if single or multiple flagella of *E. coli* rotates in clockwise (CW) direction. In essence, multi-flagellated mechanism is an intricate interplay between geometric nonlinearity, hydrodynamics, and contact.

Inspired by the complexity of mechanics behind simple locomotion, mechanical engineers also tried to formulate the motion of multi-flagellated bacteria.^{15,23–25} It was only until recently that the bundling behavior was shown to be a purely mechanical phenomenon that is due to the interaction of the soft helical structures and the viscous fluid.¹⁵ Besides its complexity in physics, the multi-flagellated mechanism is important from both robotic and biological perspectives due to the following features : (1) directional stability,² (2) redundancy of actuation,²⁶ (3) chemical secretion using flagella,^{27,28} (4) improved efficiency in swarm and propagation^{29,30}

Prior works on soft robots actuated by flagella have considered both simulation and experiments. To solve this fluid-structure interaction problem, computational fluid dynamics model and slender body theory (SBT) were used to predict the motion of single flagellated small-scale robot with rigid flagellum,^{31,32} ignoring the effect of flexibility of the flagella. With recent advancements

in computational capability, the structural flexibility in a single-flagellated system can also be accounted for,^{33–35} the flagellum can be modeled as a linear elastic Kirchhoff rod.³⁶ Multiple studies have demonstrated the modeling of multi-flagellated systems.^{37–42} However, the coupling between long-range hydrodynamics, geometrically nonlinear deformation, and contact, has not been accounted for until recently.⁴³

In the field of microbots, there are several studies that investigated the effect of multi-flagellated mechanism. Due to limited modes of locomotion that a single flagellated mechanism provide, Beyrand et al. presented multiple flagella microswimmers that covers rolling, running, and tumbling motion.¹⁹ Ye et al. investigated the benefit of multiple flagellated locomotion and the advantages of sinusoidal 2D geometry.²⁰ Even bio-hybrid microbots have been developed, which are created by assembly of biological flagellated organism with the man made magnetic structure, showed remarkable results of controlled locomotion using magnetic field.^{24,44} However, due to the nontrivial coupling between hydrodynamics, contact, and elasticity, researchers investigated lower order of coupling to solve the problem. e.g. (1) using rigid flagellum for flagellated robot under viscous fluid,^{31,32} (2) using a single elastic flagellum without modeling self-contact^{33,34} or (3) using ribbon-like multiple flagella without bundling

behavior.^{19,20} Overall, a comprehensive numerical model and physical prototype for flagellar bundling still needs further investigation.

In this paper, we present a macroscopic soft robotic platform based on propulsive mechanism of flagellated micro-organisms and a physics-based computational framework to simulate the robot. The computational tool uses the Discrete Elastic Rods (DER) algorithm for elastic rod dynamics, Regularized Stokeslet Segments (RSS) method for hydrodynamics including long-range interaction,¹⁷ and Spillman and Teschner's method of contact.⁴⁵ We first verify the simulation against the experiments with qualitative and quantitative comparison. As shown in Figure 1, the experiment and simulation show good qualitative agreement; the simulation successfully captures the attraction between two flagella arising from hydrodynamic interaction. Following quantitative comparison between experiments and simulations, the shortcomings of the model are discussed and directions for future research are suggested. We find from experiments and simulations that the flagellar buckling⁴⁶ does not occur for the multiflagellated mechanism, while a single flagellated system may undergo buckling due to excessive hydrodynamic loads. An efficiency comparison between a single- and a multi-flagellated system shows that the single-flagellated robot has a slight efficiency advantage over its multi-flagellated counterpart. This simulation and the observations on the propulsive mechanism will set the foundation for further developing the soft robotic prototype. Eventually, we expect that the robotic prototype can be miniaturized towards a microbot that harnesses structural flexibility and hydrodynamic interaction for functionality.

2. Methods

2.1. Experimental setup

For experimental data collection, we used glycerin as the viscous medium for our robot. A cylindrical tank with diameter of 28 cm and height of 45 cm was used with glycerin filled up to a height of approximately 40 cm of the tank. The robot was initially placed at the center of the glycerin tank to remain approximately 10 cm apart from the sidewalls. For every experiment, tem-

perature and viscosity were measured. Viscosity was measured using USS-DVT4 rotary viscometer and the viscosity measurement was in a good agreement with the nominal value of the glycerin; dynamic viscosity of $\mu = 0.956 \pm 0.2$ Pa.s. The temperature of glycerin was approximately 22°C throughout the experiment to minimize the effect of temperature on viscosity. The fluid was mixed thoroughly before the experiment to avoid variation in density inside the tank.

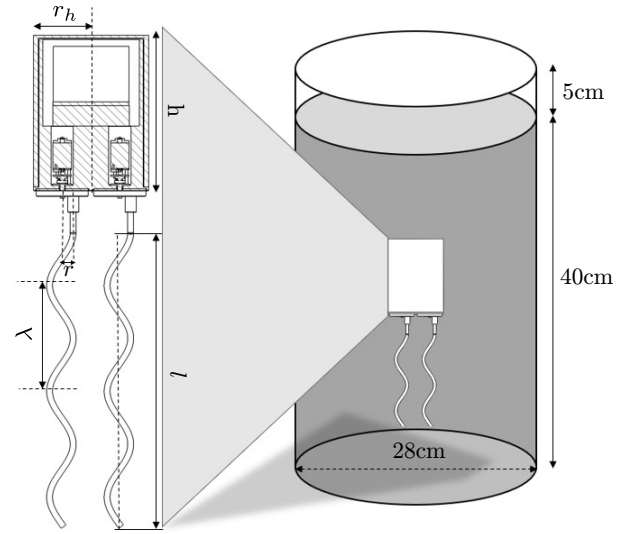


Figure 2. Experimental set up, robot schematic and symbol notation

The robot head contained Wemos D1 mini micro controller unit used for the motor control, two 3.7 V 500 mAh Lipo batteries, and two mini geared DC motors. The motor was calibrated for angular velocity using Cybertech DT6236B Tachometer. PWM-RPM was calibrated within $\pm 1(0.01\%)$ rpm at 3.8 V. The head is in cylindrical shape with radius of 3.1 ± 0.01 cm and height ($h = 8.2 \pm 0.01$ cm) and was built using fused deposition modeling (FDM) 3D printer with polylactic acid plastic (PLA) material ($\rho = 1.26$ g/cm³). The robot head was comprised of the casing and the main body. Urethane wax was applied inside of the casing, outside of the main body, and the motor chamber to further prevent the glycerin from penetrating into the robot. Ballast was placed near the robot centroid for neutral buoyancy and weight balance. Flagella were attached on the bottom plates that are connected to the motors.

Parameter	Value(Exp/Sim)	Description
r	0.0064	Radius of helix (m)
λ	0.0572	Pitch of helix (m)
l	0.0954	Axial length of helix (m)
r_h	0.031	Radius of robot head (m)
r_0	0.0016	Radius of the rod (m)
E	1.255×10^6	Young's Modulus (Pa)
ν	0.5	Poisson's Ratio
ρ	1260	Density (kg/m ³)
μ	$0.956 \pm 0.2 / 1.0$	Viscosity (Pa·s)
Δt	1.0×10^{-4}	Time step
ϵ	1.67×10^{-4}	Regularization parameter
$ e $	5.0×10^{-3}	Discretization length (m)
C_t	4.8	Translational drag coefficient
C_r	0.36	Rotational drag coefficient

Table 1. Table of geometric, physical and simulation parameters with symbol representations

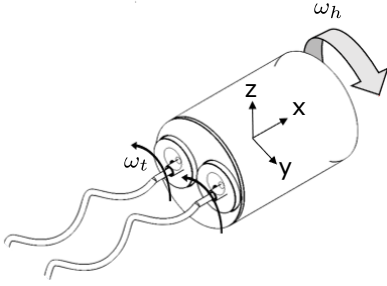


Figure 3. Schematics of robot with relevant motion. ω_h and ω_t represents head and tail rotational velocity respectively.

For the flagella, VPS elastomeric material was used for fabrication with Young's modulus $E = 1255 \pm 49$ kPa and Poisson's ratio $\nu \approx 0.5$ (i.e. nearly incompressible). Catalyst and base – both liquid – were mixed with 1:1 volume ratio. Iron fillings were added to the liquid mixture to match the density of the glycerin ($\rho = 1.26$ g/cm³). Left handed helix shaped molds with different pitch parameters ($\lambda = 3.18, 4.45, 5.72$ cm) were 3D printed. Hollow PVC tubes were placed inside the molds and the liquid mixture was injected inside the tubes. After waiting a few hours to cure, the PVC tubes were cut out and filamentary soft helical rods were obtained.⁴⁷

For data processing, we captured the video of the robot submerged inside the glycerin tank over 300 seconds. Out of the 300 seconds, we used the data between 30 seconds and 270 seconds to ignore the initial transience during the speed ramp-

up from 0 rpm to a prescribed total rpm. Then, we converted the videos into jpg files with frame rate of 1 frame per second. The image files were then processed by ImageJ image processing tool using stacked image processing centroid calculation.

2.2. Physics based simulation of the soft robot

Figure 4 shows the discretized schematic of our robot. The rod is discretized into N nodes: $\mathbf{x}_k = [x_k, y_k, z_k]^T$ for $0 \leq k \leq N - 1$. and $N-1$ corresponding edges: $\mathbf{e}^k = \mathbf{x}_{k+1} - \mathbf{x}_k$ for $0 \leq k \leq N - 2$. The degree of freedom (DOF) vector of discretized robot is defined as $\mathbf{q} = [\mathbf{x}_0^T, \theta^0, \mathbf{x}_1^T, \theta^1, \dots, \mathbf{x}_{N-2}^T, \theta^{N-2}, \mathbf{x}_{N-1}^T]^T$, where θ^k is the scalar twist angle at edge \mathbf{e}^k . Therefore, the size of the DOF vector for N nodes is $4N - 1$. Hereafter, subscripts are used for the node-based quantities and superscripts are used for the edge-based quantities.

An important characteristic of the DER method is computation of the twisting of a rod simply by using a set of single scalar quantities θ^k embedded in the DOF vector. In this formulation, each edge has a reference frame (noted as $\mathbf{d}_1^k, \mathbf{d}_2^k, \mathbf{t}^k$ in Figure 4) that is orthonormal and adapted (i.e. \mathbf{t}^k is the tangent along the k -th edge). The construction of reference frame is first initialized at the first edge ($k = 0$) at time $t = 0$ with an arbitrary set of orthonormal vectors (with the condition that the third vector \mathbf{t}^0 is the tangent to the first edge). Then, the reference frame is parallel transported⁴⁸ to the subsequent edges to form

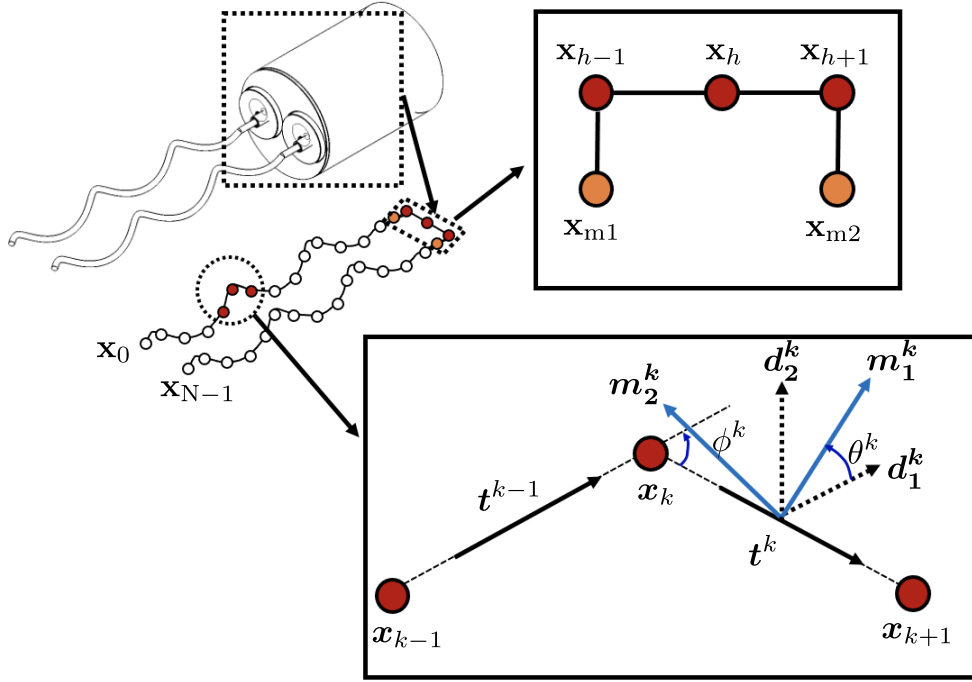


Figure 4. Discretization schematics of the soft robot DER formulation. Superscript denotes edge based quantities and subscript denotes node base quantities. Head part was modeled into three nodes, in the center of the head part is x_h , the left and right of the center head node; x_{h-1} , are denoted as red dots. x_{h+1} . Two orange dots represent x_{m1} , and x_{m2} which are the nodes where the flagella is actuated

the reference frame on all the edges. After this initialization, reference frame can be updated at each time step by parallel transporting d_1^k , d_2^k , t^k from the “old” configuration (DOF vector before the time step) to the “new” configuration (DOF vector after the time step). The material frame is also an adapted orthonormal frame (noted as m_1^k , m_2^k , t^k in Figure 4) that is identical to the reference frame at $t = 0$. Since both the frames share a common director (t^k), a single scalar quantity – the twist angle, θ^k – can be used to compute the material frame from the reference frame. Algorithmic representation of this update of frame is shown in Algorithm 1.

Based on the discretization, the elastic strains are required to calculate the energy and formulate the equations of motion (EOM) to march from time $t = t_i$ to time $t = t_{i+1} = t_i + \Delta t$, where Δt is the time step size in the simulation outlined in Algorithm 1. An elastic rod has three types of strains – bending, twisting, and stretching – associated with its deformation. Using these strains, we can calculate stretching, bending and twisting energy of our system; the sum of three energy is noted as the elastic energy and is represented as

Eq.1. Details on calculation of the strains and energy term can be found on **Supplementary methods section S1**.

$$E_{\text{elastic}} = \underbrace{\sum_{k=0}^{N-2} E_k^s}_{\text{stretching energy}} + \underbrace{\sum_{k=1}^{N-2} E_k^b}_{\text{bending energy}} + \underbrace{\sum_{k=1}^{N-2} E_k^t}_{\text{twisting energy}}, \quad (1)$$

We can simply take the gradient of the energy terms with respect to the DOFs to get the elastic force at each DOF. The elastic force at the k -th DOF is $-\frac{\partial E_{\text{elastic}}}{\partial \mathbf{q}_k}$. The simulation marches forward in time by updating the configuration, i.e. DOF vector, of the robot based on EOM. We can even impart artificial configuration updates in the simulation that are dynamic. In particular, for actuation of the robot we implement a time-dependent fixed rate natural twist on nodes x_{m1} , and x_{m2} shown in Figure 4. In order to propagate in time, the equation of motion to be solved at the k -th node is

$$\mathbf{f}_k \equiv \frac{m_k}{\Delta t} \left[\frac{\mathbf{q}_k(t_{i+1}) - \mathbf{q}_k(t_i)}{\Delta t} - \dot{\mathbf{q}}_k(t_i) \right] + \frac{\partial E_{\text{elastic}}}{\partial \mathbf{q}_k} - \mathbf{f}_k^{\text{ext}} = 0, \quad (2)$$

where $\mathbf{q}_k(t_i)$ is the old position (and the k -th element of the vector $\mathbf{q}(t_i)$), $\dot{\mathbf{q}}_k(t_i)$ is the old velocity, m_k is the lumped mass at the k -th DOF, and $\mathbf{f}_k^{\text{ext}}$ is the external force on the k -th DOF. Note that Eq.2 is simply a statement of Newton's second law. External forces may include gravity, contact, and hydrodynamics and the $(4N-1)$ -sized external force vector can be written as

$$\mathbf{f}^{\text{ext}} = \mathbf{f}^h + \mathbf{f}^{\text{head}} + \mathbf{f}^c, \quad (3)$$

where \mathbf{f}^h is the hydrodynamic force vector on the flagella, \mathbf{f}^{head} is the hydrodynamic force vector on the head, and \mathbf{f}^c is the contact force vector. (**Supplementary methods section S2**)

Now that the EOM is defined, we need to solve the system of $(4N-1)$ equations defined by Eq. 2 to compute the new position vector, $\mathbf{q}(t_{i+1})$. Newton-Raphson method can be used to solve the equations which requires the Jacobian of Eq.2. The (k, m) -th element of the square Jacobian matrix is

$$\mathbb{J}_{km} = \frac{\partial \mathbf{f}_k}{\partial \mathbf{q}_m} = \mathbb{J}_{km}^{\text{inertia}} + \mathbb{J}_{km}^{\text{elastic}} + \mathbb{J}_{km}^{\text{ext}}, \quad (4)$$

The expressions for the Jacobian terms associated with the elastic forces are available in the literature.⁴⁸ The Jacobian terms associated with some external forces ($\mathbf{f}^h, \mathbf{f}^{\text{head}}$) cannot be analytically evaluated and those terms are simply set to zero. In other words, those forces are incorporated into the simulation in an Euler forward fashion.

After solving Eq. 2 to calculate the new position $\mathbf{q}_k(t_{i+1})$, new velocity can be trivially computed from $\dot{\mathbf{q}}_k(t_{i+1}) = (\mathbf{q}_k(t_{i+1}) - \mathbf{q}_k(t_i)) / \Delta t$.

Algorithm 1 Multiflagella soft robot simulation

Require: $\mathbf{q}(t_j), \dot{\mathbf{q}}(t_j)$
Require: $(\mathbf{d}_1^k(t_j), \mathbf{d}_2^k(t_j), \mathbf{t}^k(t_j))$
Ensure: $\mathbf{q}(t_{j+1}), \dot{\mathbf{q}}(t_{j+1})$
Ensure: $(\mathbf{d}_1^k(t_{j+1}), \mathbf{d}_2^k(t_{j+1}), \mathbf{t}^k(t_{j+1}))$

- 1: Guess : $\mathbf{q}^{(1)}(t_{j+1}) \leftarrow \mathbf{q}(t_j)$
- 2: $n \leftarrow 1$
- 3: Calculate \mathbf{f}^h and \mathbf{f}^{head}
- 4: ▷ **Supp. methods - sec. S2**
- 5: solved $\leftarrow 0$
- 6: **while** solved == 0 **do**
- 7: **while** error > tolerance **do**
- 8: Compute ref. frame using $\mathbf{q}^{(n)}(t_{j+1})$
- 9: $(\mathbf{d}_1^k(t_{j+1}), \mathbf{d}_2^k(t_{j+1}), \mathbf{t}^k(t_{j+1}))^{(n)}$
- 10: Compute ref. twist $\Delta m_{k,\text{ref}}^{(n)}$
- 11: Compute material frame
- 12: $(\mathbf{m}_1^k(t_{j+1}), \mathbf{m}_2^k(t_{j+1}), \mathbf{t}^k(t_{j+1}))^{(n)}$
- 13: Compute \mathbf{f} and \mathbb{J} ▷ Eq. 2, 4
- 14: $\Delta \mathbf{q} \leftarrow \mathbb{J} \backslash \mathbf{f}$
- 15: $\mathbf{q}^{(n+1)} \leftarrow \mathbf{q}^{(n)} - \Delta \mathbf{q}$
- 16: error $\leftarrow \text{sum}(\text{abs}(\mathbf{f}))$
- 17: $n \leftarrow n + 1$
- 18: **end while**
- 19: solved $\leftarrow 1$
- 20: **for** $l = 0$ to $l = N - 2$ **do**
- 21: **for** $m = 0$ to $m = N - 2$ **do**
- 22: Compute $\delta_{(l,m)}^{\text{min}}$
- 23: **if** $\delta_{(l,m)}^{\text{min}} < 2r_0$ **then**
- 24: Compute $\mathbf{f}_l^c, \mathbf{f}_{l+1}^c, \mathbf{f}_m^c, \mathbf{f}_{m+1}^c$
- 25: ▷ **Supp. methods - sec. S3**
- 26: solved $\leftarrow 0$
- 27: **end if**
- 28: **end for**
- 29: **end for**
- 30: **end while**
- 31: $\mathbf{q}(t_{j+1}) \leftarrow \mathbf{q}^{(n)}(t_{j+1})$
- 32: $\dot{\mathbf{q}}(t_{j+1}) \leftarrow \frac{\mathbf{q}(t_{j+1}) - \mathbf{q}(t_j)}{\Delta t}$
- 33: $(\mathbf{d}_1^k(t_{j+1}), \mathbf{d}_2^k(t_{j+1}), \mathbf{t}^k(t_{j+1}))$ ←
 $(\mathbf{d}_1^k(t_{j+1}), \mathbf{d}_2^k(t_{j+1}), \mathbf{t}^k(t_{j+1}))^{(n)}$

3. Results and Discussion

3.1. Validation of Physics-based Simulation of Multi-flagellated robot

To demonstrate the validity of our simulation model, we investigated the locomotion of our multi-flagellated robot. Figure 5.a shows snapshots from experiments and simulations at three

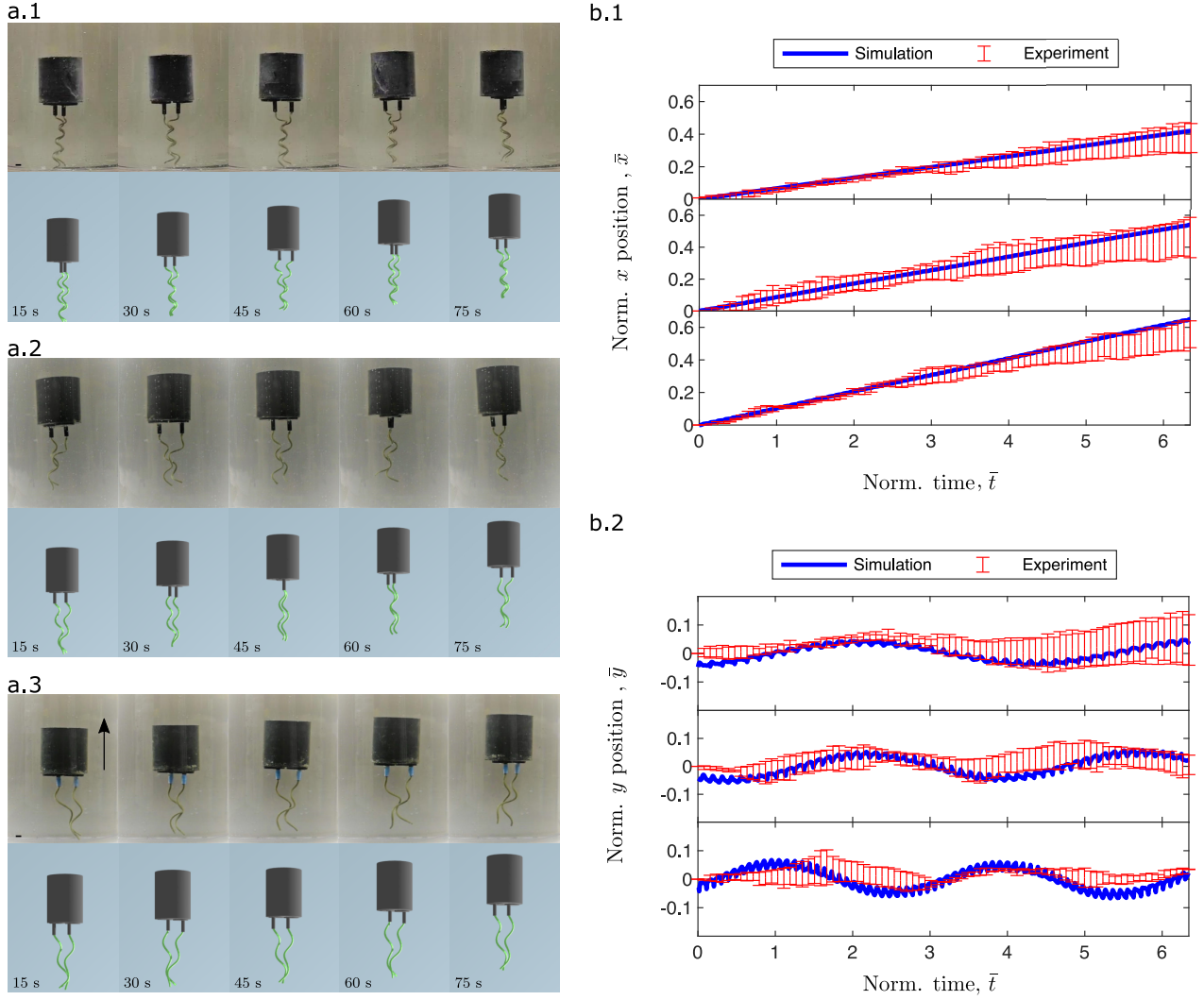


Figure 5. Comparison of data for experiment and simulation for different pitch to helix radius ratio of flagella ($\bar{\lambda} = 5, 7, 9$) : (a) Snapshot comparison between experiment and simulation at 60 rpm, scale bar: 1cm ; (b) Comparison of experimental data with simulation at 30, 40, 50 rpm for $\bar{\lambda} = 7$. (b.1) shows comparison of normalized x position and (b.2) shows comparison of normalized y position against normalized time

different values of pitch: $\bar{\lambda} = \{5, 7, 9\}$. From Figure 5.a, we first qualitatively analyze the match between the transitional motion of the flagella crossing and bundling behavior. We noted during experimental observations that $\bar{\lambda} = 5$ case formed a bundle throughout the entire range of angular velocity variation (30 to 70 rpm). On the other hand, $\bar{\lambda} = 7$ case formed a partial bundle at 50 and 60 rpm, and $\bar{\lambda} = 9$ did not bundle but had continuous contact between two flagella. In Figure 5.b, we present quantitative comparison of experimental data with simulation at 30, 40, and 50 rpm for $\bar{\lambda} = 7$ and plot the position of the robot along x and y directions against normalized time. The data frequency of the experiment is 1 frame per second (fps) and the data frequency of simulation is 10 fps.

We obtain the values of the numerical prefactors C_t and C_r by data fitting using data obtained on experiment with $\bar{\lambda} = 7$. By comparing the mean total least squared error for the axial velocity v , rotational velocity, the prefactors that provided minimal error between experiment and simulation were used. Both prefactors are the coefficients to account for non-spherical shape of the robot body in translational, rotational hydrodynamic drag calculation based on sphere at Stokes flow.

The experiment and simulation results show agreement in the positional data for both \bar{x} and \bar{y} in Figure 5.b. The normalized x position, \bar{x} , in particular, shows a good match between the simulation and experiment (Figure 5.b.1). From Figure 5.b.2, we can observe that as the angular ve-

locity increases, the oscillation frequency in normalized y position increases accordingly. This represents an undulatory sideways motion of the robot as its is moving upward (along x direction). Even though both experiments and simulations show the same trend, there exist discrepancies in the higher rpm and lower normalized pitch cases. We attribute this to the friction between the flagellar surfaces. Unlike simulation where we resolve contact between the two flagella without consideration on friction between each flagellum, we observed in our experiment that once it partially or fully bundles, the bundled part had high frictional force that makes the flagella to be kept in bundled configuration when transitioning to partially bundled regime.

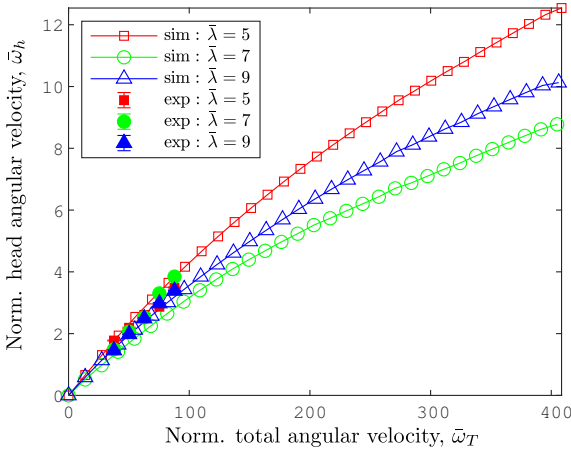


Figure 6. Comparison of simulation and experiment for head and tail angular velocity.

Simple moment balance tells us that the cell body (i.e., the head of the robot) and the flagella have to rotate in opposite directions for net zero torque. It is known through previous works that the counter rotation of cell body in bacterial locomotion contributes to the trajectory and efficiency of the organism and could even contribute to the bundling of the flagella.^{49,50} We use our robot to investigate the rotation of the head and, in Fig. 6, plot the angular velocity of the head as a function of the total angular velocity from both experiments and simulations at three different values of pitch. At lower values of total angular velocity ($\bar{\omega}_T \lesssim 100$), there is little variation in the angular velocity of the head at different values of pitch. In both experiments and simulations, we see that the angular velocity of the head increases almost linearly with the total angular velocity. We ex-

ploit our simulations to probe the higher angular velocity regime and clearly see that the head angular velocity increases sublinearly with the total angular velocity. The variation in the head angular velocity as a function of the pitch of the flagella is worth mentioning. Among the three examined here ($\bar{\lambda} = \{5, 7, 9\}$), the head angular velocity is the highest at $\bar{\lambda} = 7$. This nonlinear dependence on the geometric parameter (pitch) of the flagella may be counter intuitive; however, it is a manifestation of the highly nonlinear and coupled nature of the problem. This type of nonlinearity with variation of geometry can be also be found in Ref.¹⁴ that used a single-flagellated system and analyzed the normalized force with respect to the normalized pitch.

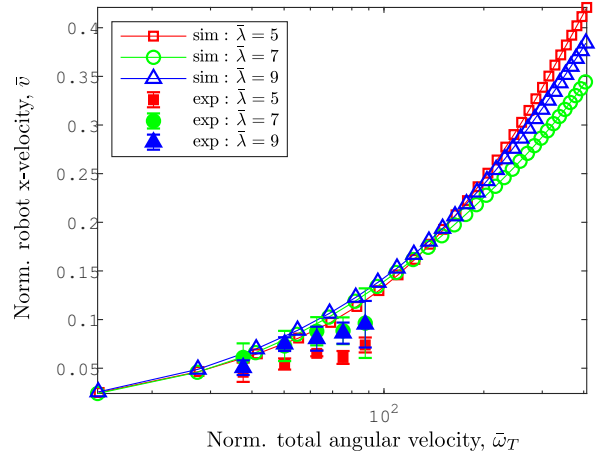


Figure 7. Non-linear relationship of angular velocity and robot x-velocity captured through simulation. The experimental data are in symbol with error bars.

Next, in Figure 7, the velocity of the bacteria robot along the x -axis is shown as a function of the normalized total angular velocity, $\bar{\omega}_T$. Interestingly, the translational velocity increases superlinearly with the total angular velocity in the regime explored here. The nonlinear dependence of translational velocity on the pitch of the flagella is also obvious. The case with $\lambda = 7$ results in lower propulsive speed compared with the $\lambda = 5$ and $\lambda = 9$ cases. In Figure 7, the simulation results overestimate the velocity of the experimental robot.

This can be attributed to the friction between the two flagella that was observed in experiments. Since the amount of contact is more dominant at lower values of pitch, the experiments and the simulations differ further for the case with $\bar{\lambda} = 5$

compared with $\bar{\lambda} = 7$ and $\bar{\lambda} = 9$ cases. The simulation tool, at this stage of our research, enforces non-penetration condition but does not incorporate friction. This implies that one flagellum can smoothly slide past another flagellum without any resistance from friction. However, that is not the case in the real world. In experiments, the flagella form a tighter bundle compared with simulations which leads to a lower net propulsive force forward. Incorporating physically-accurate friction inside low Reynolds environment is a direction of future research. The simulation tool presented in this paper, that models the entire system as a single rod for computational efficiency, can be used to explore various models of friction and eventually formulate an accurate model that matches experiments. A few recent works have explored friction among rods in simpler settings^{51,52} and our simulations can be augmented to include such friction models.

3.2. Comparison with Single-Flagellated Robot

In this section, we take one step towards a mechanistic understanding of the difference between these two modes of locomotion – single-flagellated and multi-flagellated. Locomotion of a robot (or bacterium) with single flagellum was recently investigated using a DER-based numerical framework.³⁴ A single-flagellated robot cannot exhibit bundling; however, it can undergo buckling instability beyond a critical value of the total angular velocity when the resulting external hydrodynamic force is too large. In Figure 8, we utilize our same simulation tool to model a single-flagellated robot.

We assumed that all the parameters are the same between the single-flagellated robot and the multi-flagellated case discussed above. The only difference is the number of flagella. Figure 8.a shows the Euclidean distance, L' , between the head node and the tail node (the node at the free tip of the flagellum) as a function of the total angular velocity, ω_T , obtained from simulations. This apparent length, L' , has been normalized by its value at $\omega_T = 0$ so that all the curves for three different values of pitch start at $(0, 1)$. The star symbols represent the angular velocity beyond which the apparent length, L' , of the robot abruptly drops and the flagellum buckles. Two snapshots – one of

an unbuckled configuration and one of a buckled shape – are also shown on Figure 8.a. For $\bar{\lambda} = 5$, the flagella buckles at $\bar{\omega}_T \approx 230$ and the $\bar{\lambda} = 7$ case buckles at $\bar{\omega}_T \approx 363$. The case for $\bar{\lambda} = 9$ does not buckle in the regime explored in this figure. The findings on single-flagellated robot are similar to the study in Huang et al.³⁴

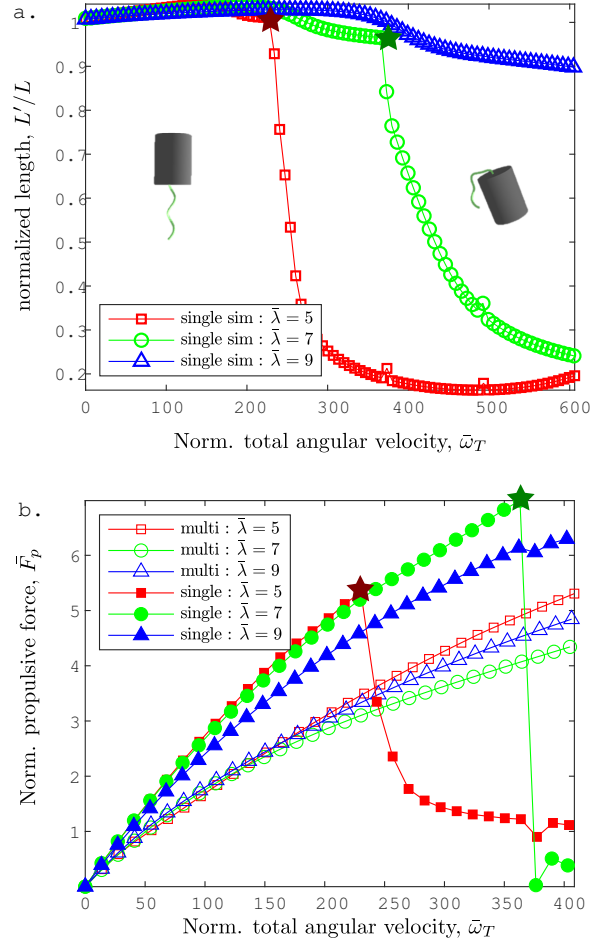


Figure 8. Comparison between single-flagellated robot and multi-flagellated robot simulation: (a) Plot of normalized tail to head distance with respect to normalized angular velocity. Star symbols represent the critical angular velocity where the flagellum buckles. Rendered image of unbuckled (left), and buckled (right) state of the robot shown within the graph. (b) Figure of normalized propulsive force with respect to normalized angular velocity. Star symbols represent the buckling. The multi flagellated case does not exhibit buckling behavior.

Next, we employ the simulation tool to comparatively explore the propulsive forces of the two types of systems – single-flagellated and multi-flagellated. Figure 8.b shows the non-dimensionalized propulsive force as a function of total angular velocity at three different values of pitch for both the single-flagellated and multi-flagellated cases. Propulsive force is de-

defined as the x -component (direction of motion of the robot) of the force exerted on the head (Eq. 15, Supplementary methods section S2). The propulsive force for the multi-flagellated robot was divided by the number of flagella. The propulsive force generated by the robot is small (on the order of 10^{-3} N), which makes it difficult to experimentally measure. Our robotic platform does not have a force sensor and, therefore, we use simulations to analyze the propulsive force and efficiency of the soft robot. The trend is qualitatively different between the two cases. For single-flagellated robot buckles at a critical angular velocity (indicated by star symbols) and its propulsive force dramatically drops at that point. Multi-flagellated robot does not exhibit buckling behavior even at larger angular velocities; the flagella bundle instead. A point of note is the relatively larger propulsive force per flagellum in the single-flagellated robot prior to buckling than the multi-flagellated robot. The propulsive force depends on the deformed shape of the flagella and this shape differs between the single-flagellated case (no bundling, only buckling) and multi-flagellated case (prominent bundling). However, beyond the critical threshold for buckling in a single-flagellated robot, the propulsive force is larger in the multi-flagellated system. In short, single-flagellated robot generates larger propulsive force per flagellum; however, its propulsion is limited by an instability. The non-monotonic dependence of propulsion force on the geometry of the flagella (pitch) is observed in the multi-flagellated case. The robot with $\bar{\lambda} = 5$ generates the largest force and $\bar{\lambda} = 7$ generates the least; $\bar{\lambda} = 9$ falls in between. In contrast, a single-flagellated robot generates more propulsion as the pitch decreases. However, this observation is true only for the range of parameters explored in this study. Prior works¹⁴ show non-monotonic dependence of propulsion on the pitch of the flagellum; however, the flagellum was assumed to be rigid.

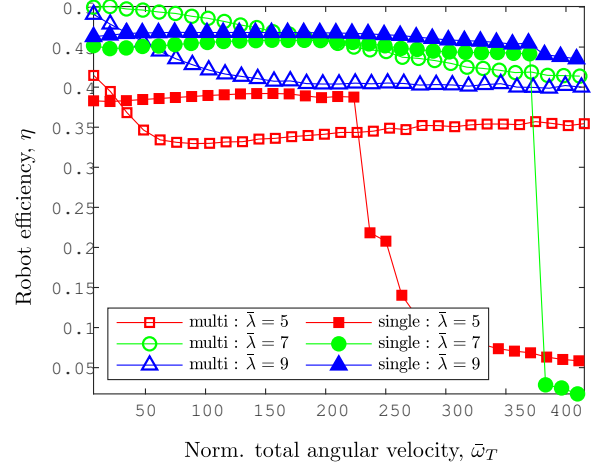


Figure 9. Efficiency graph for the single, and multi flagella robot simulation. Efficiency is defined as the ratio of the force and torque of the head. Due to flagella interaction multi-flagellated robot has lower efficiency.

The observations on propulsive force lead us to address the efficiency of the flagellated robots using numerical simulations. Figure 9 shows the variation of efficiency with the total angular velocity at three values of pitch in both the cases. Efficiency is defined as $\eta = \frac{f_h^{\text{head}} \cdot r_h}{T_h}$, where f_h^{head} is the hydrodynamic force on the head, and T_h is the torque due to rotation of the head. Qualitatively, efficiency is a measure of the ratio of the propulsive force and the torque exerted by the motor. At smaller values of angular velocity, multi-flagellated robot decreases in efficiency. This decrease is particularly prominent at small values of pitch and, thus, high interaction between flagella. Efficiency is the highest when $\bar{\lambda} = 7$ and lowest at $\bar{\lambda} = 5$, which further signifies the nonlinear nature of the problem. If the robot has a single flagellum, there is no bundling and the shape of the flagellum remains almost helical until the threshold for buckling. Therefore, the efficiency remains almost constant as a function of angular velocity before buckling. The efficiency drops to almost zero post buckling.

4. Conclusion

In conclusion, we presented a multi-flagellated soft robotic platform and a numerical simulation method. These tools were used to explore the relationship between the motion of the robot and the geometry of the flagella. Both the experiments and simulations could capture the

bundling behavior of the elastic flagella caused by long range hydrodynamic interaction. Bundling is only possible if the flagella are flexible and there is long range interaction by flows induced by distant parts of the flagella. Prior works often neglected the flexibility of the flagella or ignored the long range hydrodynamics in favor of simplified (but computationally cheap) resistive force theory-based hydrodynamic model.¹ Our study emphasizes the need to accurately capture these two ingredients – flexibility and long range hydrodynamics – in modelling bacteria and robots inspired by them. The simulation tool can successfully capture both the ingredients.

The accuracy of the simulation when compared to the experiment was reasonable, where our metrics for comparison were the translational velocity of the robot and the angular velocity of the head. Lack of an accurate friction model was identified as the main reason behind any mismatch between experiments and simulations. This simulation and the experimental platform gives a basis for the future development of multiple flagella based robots. The results were presented in non-dimensional format and, as long as the dimensionless groups are the same (e.g., low Reynolds number is low), they apply to robots and organisms of any size.

The robotic platform can be easily repurposed to explore tumbling – change in direction of swimming – when one flagellum rotates in a direction opposite to the other flagellum. In addition, the robot can be improved by integrating sensors and inertial measurement unit (IMU) to achieve 3D trajectory control of the robot.

Directions for future work include (1) analysis of the tumbling behavior, (2) incorporation of physically accurate friction model, and (3) formulation of control policy along with hardware improvement for an autonomous robot. Despite these limitations, we are close to realizing palm-sized flagellated robots that are simple in design (few moving part) and control (angular velocity is the only control input) yet functional (i.e., capable of following 3D trajectory by bundling and tumbling). With the ongoing advancements in material science and nano fabrication in creating tiny rotational actuators, we envision that our research, in the long term, can lead to small, simple, cheap

but functional microbots for environmental monitoring, drug delivery, and inspection of engineering assets in hazardous and hard-to-reach locations.

Acknowledgements

We are grateful for the financial support from the National Science Foundation (Award numbers: IIS-1925360, CMMI-2053971, CAREER-2047663) and the Henry Samueli School of Engineering and Applied Science, University of California, Los Angeles.

Author Disclosure Statement

Authors declare that they have no conflict of interest.

References

- ¹ B. Y. J. Gray and G. J. Hancock, “The Propulsion of Sea-Urchin Spermatozoa,” *Journal of Experimental Biology*, vol. 32, no. 4, pp. 802–814, 1955.
- ² H. C. Berg and D. A. Brown, “Chemotaxis in *E. coli* analysed by 3D tracking,” *Nature*, vol. 239, pp. 500–504, 1972.
- ³ J. Lighthill, “Flagellar Hydrodynamics : The John von Neumann Lecture,” *Society for Industrial and Applied Mathematics*, vol. 18, no. 2, pp. 161–230, 1975.
- ⁴ C. Brennen and H. Winet, “Fluid Mechanics of Propulsion by Cilia and Flagella,” *Annual Review of Fluid Mechanics*, vol. 9, no. 1, pp. 339–398, 1977.
- ⁵ E. M. Purcell, “Life at low Reynolds number,” *American Journal of Physics*, vol. 45, no. 1, pp. 3–11, 1977.
- ⁶ R. E. Johnson and C. J. Brokaw, “Flagellar hydrodynamics. A comparison between resistive-force theory and slender-body theory,” *Biophysical Journal*, vol. 25, no. 1, pp. 113–127, 1979.
- ⁷ K. Son, J. S. Guasto, and R. Stocker, “Bacteria can exploit a flagellar buckling instability to change direction,” *Nature Physics*, vol. 9, no. 8, pp. 494–498, 2013.

- ⁸ N. C. Darnton, L. Turner, S. Rojevsky, and H. C. Berg, "On torque and tumbling in swimming *Escherichia coli*," *Journal of Bacteriology*, vol. 189, no. 5, pp. 1756–1764, 2007.
- ⁹ H. C. Berg, *E. coli in Motion*. Springer Science & Business Media, 2008.
- ¹⁰ H. C. Berg, "The rotary motor of bacterial flagella," *Annual review of biochemistry*, vol. 72, 2003.
- ¹¹ M. Silverman and M. I. Simon, "Bacterial flagella," *Encyclopedia of Microbiology*, no. 24, pp. 398–409, 1977.
- ¹² R. Meadows, "How bacteria shift gears," *PLoS Biology*, vol. 9, no. 5, pp. 9–10, 2011.
- ¹³ T. Minamino, K. Imada, M. Kinoshita, S. Nakamura, Y. V. Morimoto, and K. Namba, "Structural insight into the rotational switching mechanism of the bacterial flagellar motor," *PLoS Biology*, vol. 9, no. 5, 2011.
- ¹⁴ B. Rodenborn, C. H. Chen, H. L. Swinney, B. Liu, and H. P. Zhang, "Propulsion of microorganisms by a helical flagellum," *Proceedings of the National Academy of Sciences of the United States of America*, vol. 110, no. 5, 2013.
- ¹⁵ M. J. Kim, J. C. Bird, A. J. Van Parys, K. S. Breuer, and T. R. Powers, "A macroscopic scale model of bacterial flagellar bundling," *Proceedings of the National Academy of Sciences of the United States of America*, vol. 100, no. 26, pp. 15481–15485, 2003.
- ¹⁶ E. M. Purcell, "The efficiency of propulsion by a rotating flagellum," *Proceedings of the National Academy of Sciences of the United States of America*, vol. 94, no. 21, pp. 11307–11311, 1997.
- ¹⁷ R. Cortez, "Regularized Stokeslet segments," *Journal of Computational Physics*, vol. 375, pp. 783–796, 2018.
- ¹⁸ J. Edd, S. Payen, B. Rubinsky, M. L. Stoller, and M. Sitti, "Biomimetic Propulsion for a Swimming Surgical Micro-Robot," *IEEE International Conference on Intelligent Robots and Systems*, vol. 3, no. October, pp. 2583–2588, 2003.
- ¹⁹ N. Beyrand, L. Couraud, A. Barbot, D. Decanini, and G. Hwang, "Multi-flagella helical microswimmers for multiscale cargo transport and reversible targeted binding," *IEEE International Conference on Intelligent Robots and Systems*, vol. 2015-Decem, pp. 1403–1408, 2015.
- ²⁰ Z. Ye, S. Régnier, and M. Sitti, "Rotating magnetic miniature swimming robots with multiple flexible flagella," *IEEE Transactions on Robotics*, vol. 30, no. 1, pp. 3–13, 2014.
- ²¹ L. Zhang, J. J. Abbott, L. Dong, B. E. Kratochvil, D. Bell, and B. J. Nelson, "Artificial bacterial flagella: Fabrication and magnetic control," *Applied Physics Letters*, vol. 94, no. 6, pp. 2007–2010, 2009.
- ²² L. Turner, W. S. Ryu, and H. C. Berg, "Real-time imaging of fluorescent flagellar filaments," *Journal of Bacteriology*, vol. 182, no. 10, pp. 2793–2801, 2000.
- ²³ S. Kang and R. Maniyeri, "Numerical study on bacterial flagellar bundling and tumbling in a viscous fluid using an immersed boundary method," *Applied Mathematical Modelling*, vol. 38, no. 14, pp. 3567–3590, 2014.
- ²⁴ J. Ali, U. K. Cheang, J. D. Martindale, M. Jabbarzadeh, H. C. Fu, and M. Jun Kim, "Bacteria-inspired nanorobots with flagellar polymorphic transformations and bundling," *Scientific Reports*, vol. 7, no. 1, pp. 1–10, 2017.
- ²⁵ U. Danis, R. Rasooli, C. Y. Chen, O. Dur, M. Sitti, and K. Pekkan, "Thrust and hydrodynamic efficiency of the bundled flagella," *Micromachines*, vol. 10, no. 7, pp. 1–22, 2019.
- ²⁶ P. J. Mears, S. Koirala, C. V. Rao, I. Golding, and Y. R. Chemla, "Escherichia coli swimming is robust against variations in flagellar number," *eLife*, vol. 2014, no. 3, pp. 1–18, 2014.
- ²⁷ J. Haiko and B. Westerlund-Wikström, "The role of the bacterial flagellum in adhesion and virulence," *Biology*, vol. 2, no. 4, pp. 1242–1267, 2013.

- ²⁸ H. C. Ramos, M. Rumbo, and J. C. Sirard, "Bacterial flagellins: Mediators of pathogenicity and host immune responses in mucosa," *Trends in Microbiology*, vol. 12, no. 11, pp. 509–517, 2004.
- ²⁹ A. J. Wolfe and H. C. Berg, "Migration of bacteria in semisolid agar," *Proceedings of the National Academy of Sciences of the United States of America*, vol. 86, no. 18, pp. 6973–6977, 1989.
- ³⁰ N. A. Licata, B. Mohari, C. Fuqua, and S. Setayeshgar, "Diffusion of Bacterial Cells in Porous Media," *Biophysical Journal*, vol. 110, no. 1, pp. 247–257, 2016.
- ³¹ F. Z. Temel, A. G. Erman, and S. Yesilyurt, "Characterization and modeling of biomimetic untethered robots swimming in viscous fluids inside circular channels," *IEEE/ASME Transactions on Mechatronics*, vol. 19, no. 5, pp. 1562–1573, 2014.
- ³² A. Thawani and M. S. Tirumkudulu, "Trajectory of a model bacterium," *Journal of Fluid Mechanics*, vol. 835, pp. 252–270, 2018.
- ³³ M. Calisti, F. Giorgio-Serchi, C. Stefanini, M. Farman, I. Hussain, C. Armanini, D. Gan, L. Seneviratne, and F. Renda, "Design, Modeling and Testing of a Flagellum-inspired Soft Underwater Propeller Exploiting Passive Elasticity," *IEEE International Conference on Intelligent Robots and Systems*, no. April 2020, pp. 3328–3334, 2019.
- ³⁴ W. Huang and M. K. Jawed, "Numerical exploration on buckling instability for directional control in flagellar propulsion," *Soft Matter*, vol. 16, no. 3, pp. 604–613, 2020.
- ³⁵ M. Forghani, W. Huang, and M. K. Jawed, "Control of uniflagellar soft robots at low reynolds number using buckling instability," *Journal of Dynamic Systems, Measurement, and Control*, vol. 143, no. 6, p. 061004, 2021.
- ³⁶ G. Kirchhoff, "Über das gleichgewicht und die bewegung eines unendlich dunnen elastischen stabes," *J. Reine Angew. Math.*, vol. 56, pp. 285–313, 1859.
- ³⁷ M. Reichert and H. Stark, "Synchronization of rotating helices by hydrodynamic interactions," *European Physical Journal E*, vol. 17, no. 4, pp. 493–500, 2005.
- ³⁸ M. Kim and T. R. Powers, "Hydrodynamic interactions between rotating helices," *Physical review E*, vol. 69, no. 6, p. 061910, 2004.
- ³⁹ I. Chowdhury and S. P. Dasgupta, "Computation of Rayleigh damping coefficients for large systems," *Electronic Journal of Geotechnical Engineering*, vol. 8 C, no. January 2003, 2003.
- ⁴⁰ S. Y. Reigh, R. G. Winkler, and G. Gompper, "Synchronization and bundling of anchored bacterial flagella," *Soft Matter*, vol. 8, no. 16, pp. 4363–4372, 2012.
- ⁴¹ R. Golestanian, J. M. Yeomans, and N. Uchida, "Hydrodynamic synchronization at low Reynolds number," *Soft Matter*, vol. 7, no. 7, pp. 3074–3082, 2011.
- ⁴² H. Flores, E. Lobaton, S. Méndez-Diez, S. Tlupova, and R. Cortez, "A study of bacterial flagellar bundling," *Bulletin of Mathematical Biology*, vol. 67, no. 1, pp. 137–168, 2005.
- ⁴³ W. Huang and M. K. Jawed, "Numerical simulation of bundling of helical elastic rods in a viscous fluid," *Computers & Fluids*, vol. 228, p. 105038, 2021.
- ⁴⁴ V. Magdanz, S. Sanchez, and O. G. Schmidt, "Development of a sperm-flagella driven microbio-robot," *Advanced Materials*, vol. 25, no. 45, pp. 6581–6588, 2013.
- ⁴⁵ J. Spillmann and M. Teschner, "An adaptive contact model for the robust simulation of knots," *Computer Graphics Forum*, vol. 27, no. 2, pp. 497–506, 2008.
- ⁴⁶ M. K. Jawed, N. K. Khouri, F. Da, E. Grinspun, and P. M. Reis, "Propulsion and Instability of a Flexible Helical Rod Rotating in a Viscous Fluid," *Physical Review Letters*, vol. 115, no. 16, pp. 1–5, 2015.
- ⁴⁷ A. Lazarus, J. T. Miller, M. M. Metlitz, and P. M. Reis, "Contorting a heavy and naturally curved elastic rod," *Soft Matter*, vol. 9, no. 34, 2013.

- ⁴⁸ M. K. Jawed, A. Novelia, and O. M. O'Reilly, *A primer on the kinematics of discrete elastic rods*. Springer, 2018.
- ⁴⁹ T. R. Powers, "Role of body rotation in bacterial flagellar bundling," *Phys. Rev. E*, vol. 65, p. 040903, Apr 2002.
- ⁵⁰ M. A. Constantino, M. Jabbarzadeh, H. C. Fu, and R. Bansil, "Helical and rod-shaped bacteria swim in helical trajectories with little additional propulsion from helical shape," *Science Advances*, vol. 2, no. 11, p. e1601661, 2016.
- ⁵¹ M. Li, Z. Ferguson, T. Schneider, T. Langlois, D. Zorin, D. Panozzo, C. Jiang, and D. M. Kaufman, "Incremental potential contact: Intersection-and inversion-free, large-deformation dynamics," *ACM Transactions on Graphics*, 2020.
- ⁵² A. Choi, D. Tong, M. K. Jawed, and J. Joo, "Implicit contact model for discrete elastic rods in knot tying," *Journal of Applied Mechanics*, vol. 88, no. 5, p. 051010, 2021.

Supplementary Information for

Bacteria Inspired Multi-Flagella Propelled Soft Robot at Low Reynolds Number

Sangmin Lim, Achyuta Yadunandan and M. Khalid Jawed

*To whom correspondence should be addressed : M. Khalid Jawed.
E-mail: khalidjm@seas.ucla.edu

This PDF file includes:

- Supplementary Methods
- Figs. S1 to S2
- Legend for Movie S1
- SI References

Other supplementary materials for this manuscript include the following:

- Movie S1

Supplementary Methods

Full details of physics-based simulation for multi-flagellated soft robot.

S1. Elastic Strains, Forces and Jacobians. In order to understand the Discrete Elastic Rod algorithm (DER), it is essential to understand the elastic strains, associated energy, gradient and hessian of the energy term. As described in the main text, there are three major elastic strains that a Kirchoff rod-based formulation take into account : bending, twisting, and stretching. Bending and twisting strains are node-based quantities while stretching strain is an edge-based quantity. Bending is computed using the curvature binormal vector at each node:

$$(\kappa \mathbf{b})_k = \frac{2\mathbf{t}^{k-1} \times \mathbf{t}^k}{1 + \mathbf{t}^{k-1} \cdot \mathbf{t}^k} \quad [1]$$

The magnitude of this vector is $2 \tan(\phi_k/2)$ where ϕ_k is the turning angle shown in Figure 4. The curvature vector (i.e. bending strain) at the k -th node is then

$$\kappa_k = ((\kappa \mathbf{b})_k \cdot \mathbf{d}_2^k, -(\kappa \mathbf{b})_k \cdot \mathbf{d}_1^k). \quad [2]$$

The twist at each node is

$$\tau_k = \theta^k - \theta^{k-1} + m_{k,\text{ref}}, \quad [3]$$

where $m_{k,\text{ref}}$ represents the reference twist (i.e. twist associated with the reference frame) and can be calculated from the reference frames (1). In order to account for the rotation of the motor, we included a “natural” twist angle, $\tau_{\text{motor}} = \omega_T \cdot t$ (where t represents time), to the expression for twist at the two nodes representing the motors (\mathbf{x}_{m1} , and \mathbf{x}_{m2}) shown in Figure 4. Then the new equation for integrated twist at \mathbf{x}_{m1} and \mathbf{x}_{m2} becomes

$$\tau_k = \theta^k - \theta^{k-1} + m_{k,\text{ref}} - \tau_{\text{motor}}, \quad [4]$$

where τ_{motor} is zero everywhere except at m1 and m2. Axial stretching (ϵ^k) is an edge-based quantity, which can be represented as

$$\epsilon^k = \frac{|\mathbf{x}_{k+1} - \mathbf{x}_k|}{|\mathbf{e}^k|} - 1, \quad [5]$$

where $|\mathbf{e}^k|$ denotes undeformed magnitude of the k -th edge. The energy term associated with the elastic strains can be calculated to be

$$E_k^s = \frac{1}{2} EA (\epsilon^k)^2 |\mathbf{e}^k|, \quad [6]$$

$$E_k^b = \frac{1}{2} EI (|\kappa_k - \kappa_k^0|)^2 \frac{1}{\bar{l}_k}, \quad [7]$$

$$E_k^t = \frac{1}{2} GJ \tau_k^2 \frac{1}{\bar{l}_k}, \quad [8]$$

where $EA = E\pi r_0^2$ is the stretching stiffness, $EI = E\pi r_0^4/4$ is the bending stiffness, $GJ = G\pi r_0^4/2$ is the twisting stiffness, $G = E/(2(1+\nu))$ is the shearing modulus, and \bar{l}_k is the reference Voronoi length: $\bar{l}_k = \frac{1}{2} (|\mathbf{e}^{k-1}| + |\mathbf{e}^k|)$. The gradient of these energy terms with respect to the degree of freedom provides us with the forces associated with the energy that is required for obtaining the equation of motion. To make sure that our iteration is implicit, we can define the Jacobian terms for the components of equations of motion as,

$$\mathbb{J}_{km}^{\text{inertia}} = \frac{m_k}{\Delta t^2} \delta_{km}, \quad [9]$$

$$\mathbb{J}_{km}^{\text{elastic}} = \frac{\partial^2 E_{\text{elastic}}}{\partial \mathbf{q}_k \partial \mathbf{q}_m}, \quad [10]$$

$$\mathbb{J}_{km}^{\text{ext}} = -\frac{\partial f_k^{\text{ext}}}{\partial \mathbf{q}_m}, \quad [11]$$

where δ_{km} is the Kronecker delta function ($\delta_{km} = 1$ if $k = m$; otherwise $\delta_{km} = 0$). The expressions for the Jacobian terms associated with the elastic forces are available in the literature (1).

S2. Hydrodynamics model. We used the Regularized Stokeslet Segments method for the hydrodynamic force on the flagella and Stokes law for the hydrodynamic force on the robot head. Built on the method of regularized Stokeslets, RSS method is beneficial to reduce the sensitivity of the velocity field to the regularization parameter due to its numerical treatment of a weakly singular integral. Cortez presented this method with the assumption that the force field along a filament is piece-wise linear and suggested the possibility of application to piece-wise quadratic or higher degree polynomial (2). Importantly, RSS method accounts for the long range hydrodynamic interaction among flows induced by different nodes on the flagellum. This interaction is ignored by widely used simplified methods, also known as Resistive Force Theory (3).

Referring to Figure S1, RSS provides a relationship between the velocity at a point ($\mathbf{v}(\hat{\mathbf{x}})$ in Figure S1) and the forces applied by each node on the fluid such that

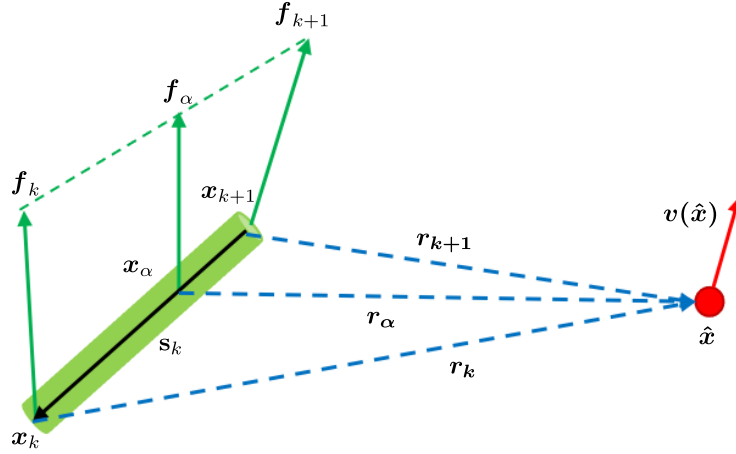


Fig. S1. Notations and discrete schematic of the flow at \hat{x} generated by a line segment.

$$8\pi\mu v(\hat{x}) = \sum_{k=0}^{N-2} (M_1^k f_k^h + M_2^k f_{k+1}^h). \quad [12]$$

where f_k^h is the force vector of size 3 that represents the force applied by the k -th node onto the fluid. This is equal and opposite to the hydrodynamic force onto the k -th node. The hydrodynamic force on the k -th node is the $4k$, $(4k+1)$, and $(4k+2)$ -th elements of the hydrodynamic force vector f^h of size $(4N-1)$ in equation 3 in the main text. The matrices (size 3×3) M_1^k and M_2^k are

$$M_2^k = |s_k|((T_{1,-1}^{k,k+1} + \epsilon^2 T_{1,-3}^{k,k+1})\mathbb{I} + T_{1,-3}^{k,k+1}(\mathbf{r}_k \mathbf{r}_k^T) + T_{2,-3}^{k,k+1}(\mathbf{r}_k \mathbf{s}_k^T + \mathbf{s}_k \mathbf{r}_k^T) + T_{3,-3}^{k,k+1}(\mathbf{s}_k \mathbf{s}_k^T)), \quad [13a]$$

$$M_1^k = |s_k|((T_{0,-1}^{k,k+1} + \epsilon^2 T_{0,-3}^{k,k+1})\mathbb{I} + T_{0,-3}^{k,k+1}(\mathbf{r}_k \mathbf{r}_k^T) + T_{1,-3}^{k,k+1}(\mathbf{r}_k \mathbf{s}_k^T + \mathbf{s}_k \mathbf{r}_k^T) + T_{2,-3}^{k,k+1}(\mathbf{s}_k \mathbf{s}_k^T)) - M_2^k, \quad [13b]$$

where, as shown in Figure S1, \hat{x} is the point of evaluation, ϵ is regularization parameter, $\mathbf{r}_k = \hat{x} - \mathbf{x}_k$, $\mathbf{s}_k = \mathbf{x}_k - \mathbf{x}_{k+1}$, \mathbb{I} is 3-by-3 identity matrix, and the scalar quantities denoted by T (e.g. $T_{1,-1}^{k,k+1}$) are described next.

$$T_{0,-1}^{k,k+1} = \frac{1}{|s_k|} \log[|s_k|R + (\mathbf{x}_\alpha \cdot \mathbf{s}_k)] \Big|_0^1, \quad [14a]$$

$$T_{0,-3}^{k,k+1} = -\frac{1}{R[|s_k|R + (\mathbf{x}_\alpha \cdot \mathbf{s}_k)]} \Big|_0^1, \quad [14b]$$

$$T_{1,-1}^{k,k+1} = \frac{R}{(|s_k|)^2} \Big|_0^1 - \frac{(\mathbf{x}_0 \cdot \mathbf{s}_k)}{(|s_k|)^2} T_{0,-1}^{k,k+1}, \quad [14c]$$

$$T_{1,-3}^{k,k+1} = -\frac{1}{R(|s_k|)^2} \Big|_0^1 - \frac{(\mathbf{x}_0 \cdot \mathbf{s}_k)}{(|s_k|)^2} T_{0,-3}^{k,k+1}, \quad [14d]$$

$$T_{2,-3}^{k,k+1} = -\frac{\alpha}{R(|s_k|)^2} \Big|_0^1 + \frac{1}{(|s_k|)^2} T_{0,-1}^{k,k+1} - \frac{(\mathbf{x}_0 \cdot \mathbf{s}_k)}{(|s_k|)^2} T_{1,-3}^{k,k+1}, \quad [14e]$$

$$T_{3,-3}^{k,k+1} = -\frac{\alpha^2}{R(|s_k|)^2} \Big|_0^1 + \frac{2}{(|s_k|)^2} T_{1,-1}^{k,k+1} - \frac{(\mathbf{x}_0 \cdot \mathbf{s}_k)}{(|s_k|)^2} T_{2,-3}^{k,k+1} \quad [14f]$$

where $\mathbf{x}_\alpha = \mathbf{x}_k - \alpha \mathbf{s}_k$, and $R = \sqrt{|\mathbf{x}_\alpha|^2 + \epsilon^2}$. Equation 12 can be used to formulate $3N$ equations (3 per node) that relate the velocities at each node with the forces applied by all the other nodes. Knowing the velocity of each node at the beginning of

the time step in DER, this linear system of equations can be solved to obtain the forces and compute the hydrodynamic force vector \mathbf{f}^h . Since the gradient of the forces with respect to the DOF vector is not available, this force is treated explicitly (Euler forward) in the simulation scheme. Complete details are found in Refs. (2) and (4).

Previously, MRS method prevailed for the analysis in low Reynolds hydrodynamics using Stokeslet methods, however, due to its dependence on the distance between contiguous cutoff functions, the choice of regularization parameter ϵ limited the accuracy of calculation. However, RSS method accounts for a continuum of regularized forces therefore decouples the necessity between discretization and the regularization. The regularization parameter used in RSS method ϵ for flagella could be interpreted as the radius of the slender filaments. Based on the analysis shown from Cortez (2) we used the regularization value of $\epsilon = 1.031 \cdot r_0 = 0.00165$ (m).

We now turn to the computation of the hydrodynamic forces on the head (\mathbf{f}^{head} in equation 3 in the main text). The middle node along the entire structure (\mathbf{x}_h in Figure 4) represents the head. As the head is translating (quantified by the velocity of \mathbf{x}_h), the viscous medium exerts a drag force onto it. The head is also rotating (quantified by the angular velocity of the head, ω_h) and the viscous fluid applies a torque to resist that rotation. We applied Stokes' law to model the hydrodynamic drag. Since Stokes' law is meant for spherical bodies and the robotic head is cylindrical, we used two numerical prefactors as fitting parameters as discussed next.

The hydrodynamic force on the head (\mathbf{x}_h) at time $t = t_{i+1}$ is

$$\mathbf{f}_h^{\text{head}} = -C_t \cdot 6\pi\mu r_h \left[\frac{\mathbf{x}_h(t_{i+1}) - \mathbf{x}_h(t_i)}{\Delta t} \right], \quad [15]$$

where C_t is a numerical prefactor to account for the non-spherical shape of the head, r_h is the radius of the head (see Table 1), and \mathbf{x}_h is the position of the head node that can be extracted from the DOF vector, \mathbf{q} . If the head is the h -th node in the structure, the vector $\mathbf{f}_h^{\text{head}}$ of size 3 represents $(4h-3)$, $(4h-2)$, and $(4h-1)$ -th elements of the vector \mathbf{f}^{head} in Eq.3. The torque due to rotation of the head is $\mathbf{T}_h = -C_r \cdot 8\pi\mu r_h^3 \omega_h$, where C_r is a numerical prefactor due to the non-spherical shape of the head and ω_h is the angular velocity of the head. The angular velocity at $t = t_{i+1}$ can be computed from the velocities of the two neighboring nodes \mathbf{x}_{h-1} , and \mathbf{x}_{h+1} (see Figure 4) such that

$$\omega_h = \frac{1}{|\mathbf{x}_{h+1}(t_{i+1}) - \mathbf{x}_{h-1}(t_{i+1})|^2} |(\mathbf{x}_{h+1}(t_{i+1}) - \mathbf{x}_{h-1}(t_{i+1})) \times [\dot{\mathbf{x}}_{h+1} - \dot{\mathbf{x}}_{h-1}]|, \quad [16]$$

where $\dot{\mathbf{x}}_{h+1} = \frac{\mathbf{x}_{h+1}(t_{i+1}) - \mathbf{x}_{h+1}(t_i)}{\Delta t}$ is the velocity of the $(h+1)$ -th node, $\dot{\mathbf{x}}_{h-1} = \frac{\mathbf{x}_{h-1}(t_{i+1}) - \mathbf{x}_{h-1}(t_i)}{\Delta t}$ is the velocity of the $(h-1)$ -th node, and \times represents vector cross product. The hydrodynamic torque is implemented in the simulation as a force-couple, i.e. a force on the node \mathbf{x}_{h-1} and an equal but opposite force on the node \mathbf{x}_{h+1} . It turns out that, in case of the specific problem studied in this paper, the magnitude of each force in the force-couple can be approximated to a very good degree as $\mathbf{T}_h / |\mathbf{x}_{h+1}(t_{i+1}) - \mathbf{x}_{h-1}(t_{i+1})|$ and the angle between two vectors in the right-side of equation 16 is 90° . The direction of the force can be approximated to be equal to $[\dot{\mathbf{x}}_{h+1} - \dot{\mathbf{x}}_{h-1}]$. The reason behind these approximations is they result in a simplified expression for the forces and allow us to take the gradient with respect to the DOFs (so that the forces are incorporated into the simulation implicitly). The resulting force on the $(h+1)$ -th node is

$$\mathbf{f}_{h+1}^{\text{head}} = -C_r \cdot 8\pi\mu \frac{r_h^3}{|\mathbf{x}_{h+1}(t_{i+1}) - \mathbf{x}_{h-1}(t_{i+1})|^2} [\dot{\mathbf{x}}_{h+1} - \dot{\mathbf{x}}_{h-1}]. \quad [17]$$

The force on \mathbf{x}_{h-1} is

$$\mathbf{f}_{h-1}^{\text{head}} = -\mathbf{f}_{h+1}^{\text{head}}. \quad [18]$$

Equations 15, 17, and 18 are used to calculate the hydrodynamic forces on the head and populate the $(4N-1)$ -sized \mathbf{f}^{head} vector. Note that this vector has only 9 non-zero elements (resulting from the forces on 3 nodes).

We fitted the parameters C_t and C_r with the experiment velocity along the x-axis which is defined in Figure 5 and head rotation speed for $\bar{\lambda} = 7$ case. The values for C_t varied from $4.9 \sim 5.1$ and C_r varied from $0.6 \sim 1.5$ for the simulation sample data. The mean total least squared error from the experimental values were the smallest for the head angular velocity when $C_r = 9$, and $C_t = 4.1$ for the x-velocity. We used these values for the head hydrodynamics for analysis of other geometric cases for flagella as well ($\bar{\lambda} = 5$, $\bar{\lambda} = 9$).

S3. Contact model. In this section, the constraint-based contact forces are explained based on the non-penetrative condition between the two edges; we refer the reader to Ref. (5) for complete details. Figure S2 shows two edge segments undergoing collision. We denote the edge segments as $S_k = (\mathbf{x}_k, \mathbf{x}_{k+1})$ and $S_m = (\mathbf{x}_m, \mathbf{x}_{m+1})$, where \mathbf{x}_k , \mathbf{x}_{k+1} , \mathbf{x}_m , and \mathbf{x}_{m+1} can be extracted from our DOF vector \mathbf{q} . In order to formulate a non-penetrative condition, penetration depth ($\epsilon_{k,m}$) is defined as the difference between the minimum Euclidean distance $\delta_{k,m}^{\text{min}}$ between S_m and S_k and sum of the radii of the segment S_k and S_m :

$$\epsilon_{k,m} = 2r_0 - \delta_{k,m}^{\text{min}}. \quad [19]$$

In our case, the radius of all the segments are the same and therefore the sum of the radii is always $2r_0$.

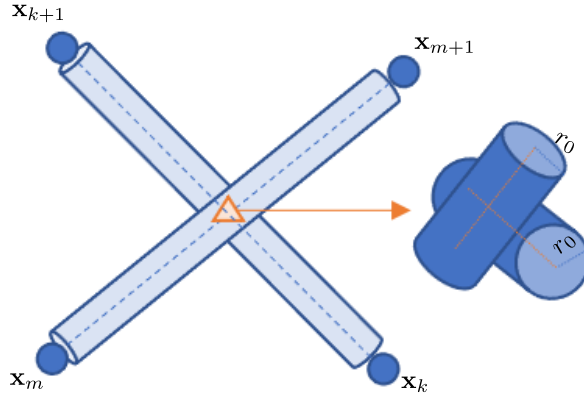


Fig. S2. Schematic of contact between two line segments S_k and S_m ; orange triangle represents point of contact, r_0 represents the radius of each rod. The minimum distance two segments cannot be smaller than $2r_0$.

A contact is detected when $\epsilon_{k,m} > 0$. The schematic shown in Figure S2 visualizes the contact condition. After detecting contact, iterations to find interference-free configuration needs to be executed. Using the detected points, the collision displacements are weighted with the barycentric coordinates of the collision such that

$$\begin{aligned}\Delta \mathbf{x}_k &= -\frac{1}{2} \mathbf{n}_{km} w_k \\ \Delta \mathbf{x}_{k+1} &= -\frac{1}{2} \mathbf{n}_{km} (1 - w_k) \\ \Delta \mathbf{x}_m &= \frac{1}{2} \mathbf{n}_{km} w_m \\ \Delta \mathbf{x}_{m+1} &= \frac{1}{2} \mathbf{n}_{km} (1 - w_m).\end{aligned}\tag{20}$$

Here, the value of $\frac{1}{2}$ represents the barycentric ratio of masses with all points having same masses, \mathbf{n}_{km} represents the minimum distance vector between S_k and S_m , w_k represents the barycentric coordinate of the contact point on the segment. Iterative process over all the detected contact positions and summing the displacement points for each \mathbf{x}_k , the displacements with mass conservation could be obtained. We use the penetration depth and compare it with the error tolerance until $\epsilon_{k,m}^{min} < \text{tolerance}$ for all the detected contact points. The contact force applied at k -th node due to collision between the contact segments S_k and S_m can be evaluated using the $\Delta \mathbf{x}_k$ values and is represented as

$$\mathbf{f}_k^c = \frac{1}{\Delta t^2} \Delta \mathbf{x}_k m_k,\tag{21}$$

where $\Delta \mathbf{x}_k$ represents weighted collision displacements with mass conservation consideration, Δt represents the time discretization, m_k represents the mass of the point (5).

While formulating the DER with contact, we found out that the level of discretization is limited by contact function. Contact method by Spillman and Teschner (5) considers the diameter of the rod so that when two nodes are within the boundary of its diameter, contact could be detected. Therefore, contact limits our length of discretized segment $|e|$ to be always greater than the diameter of the rod $2r_0$.

While the limitation in level of discretization could be a limitation, we used RSS method with our particular choice of the regularization parameter that decouples the viscous force along a line segment from discretization to overcome the limitation. It is shown by Cortez that the level of discretization has insignificant effect on the swimming speed and the trajectory waveform (2).

Movie S1. Comparison video of multi-flagellated robotic platform and simulation with flagella geometry variation

References

1. MK Jawed, A Novelia, OM O'Reilly, *A primer on the kinematics of discrete elastic rods*. (Springer), pp. 1–116 (2018).
2. R Cortez, Regularized Stokeslet segments. *J. Comput. Phys.* **375**, 783–796 (2018).
3. BYJ Gray, GJ Hancock, The Propulsion of Sea-Urchin Spermatozoa. *J. Exp. Biol.* **32**, 802–814 (1955).
4. W Huang, MK Jawed, Numerical simulation of bundling of helical elastic rods in a viscous fluid. *Comput. & Fluids* **228**, 105038 (2021).
5. J Spillmann, M Teschner, An adaptive contact model for the robust simulation of knots. *Comput. Graph. Forum* **27**, 497–506 (2008).